EES Batteries

PAPER

View Article Online
View Journal

Cite this: DOI: 10.1039/d6eb00050a

Secondary alkali-metal salts in supporting electrolytes for lithium polysulfide flow batteries

Thomas J. Leckie, [a,b] Calvin N. Turner,[b] Alan R. Kennedy,[b] Niall Dalton,[c] Pasidu Pallawela,[c] Stuart D. Robertson *[b] and Edward Brightman *[a]

Lithium polysulfide (LiPS) flow batteries are a promising next-generation technology for long-duration energy storage that offer several advantages over the more conventional lithium–sulfur configuration. Using liquid-phase polysulfides in a single-liquid flow battery configuration mitigates the polysulfide shuttle by separating most of the active material from the cell whilst enabling a higher concentration to be used, thus increasing volumetric energy density; however, performance remains limited by instability of the lithium metal anode. Alkali-metal additives have previously been shown to help regulate anode plating in lithium-metal batteries, and in the present work we investigate the effects of secondary alkali-metal bis(trifluoromethylsulfonyl)imide (MTFSI; M = Na, K, Rb, Cs) additives on the electrochemical behaviour of LiPS electrolytes under static coin cell conditions. We have synthesised a full series of MTFSI salts and report the first solvent-free crystal structure of RbTFSI, completing the family of unsolvated alkali-metal TFSI complexes. Electrochemical characterisation (CV, GCD, EIS) reveals that NaTFSI and RbTFSI improve key performance metrics, including electrolyte conductivity, capacity retention, and coulombic efficiency, despite evidence of side reactions with polysulfides. SEM-EDX analysis confirms the formation of alkali-metal and sulfurous deposits at the electrodes, indicating that parasitic reactions may dominate over the self-healing electrostatic shield (SHES) mechanism. These results demonstrate that carefully selected secondary cations, particularly Na^+ and Rb^+, can beneficially modify LiPS battery behaviour despite concurrent side reactions, providing a route toward the rational design and optimisation of electrolyte formulations for next generation LiPS flow battery technologies.

Received 3rd March 2026,
Accepted 6th May 2026

DOI: 10.1039/d6eb00050a

rsc.li/EESBatteries

Broader context

Long-duration energy storage technologies are essential for supporting a future energy system dominated by renewable electricity. Lithium polysulfide (LiPS) flow batteries are promising candidates because they use abundant sulfur and offer scalable energy capacity. Yet their development is limited by instability at the lithium metal anode, which leads to performance loss and shortened battery lifetime. This work addresses that challenge by investigating how secondary alkali-metal salts, specifically NaTFSI, KTFSI, RbTFSI, and CsTFSI, interact within LiPS electrolytes and influence battery behaviour. We focus on whether these additives can stabilise the anode or otherwise mitigate degradation processes. Our results show that sodium and rubidium salts can improve energy efficiency and cycling stability, even though they also participate in side reactions that consume some active material. The discovery of the first solvent-free crystal structure of RbTFSI further broadens understanding of electrolyte design and ion–solvent interactions. These insights are important for guiding future strategies that aim to enhance the durability of LiPS and related next-generation battery chemistries. By clarifying how secondary cations influence both beneficial and detrimental processes in LiPS systems, this study provides a foundation for more robust electrolyte formulations that could accelerate the deployment of affordable, sustainable, long-duration energy storage.

Introduction

As the demand for higher performance and lower cost batteries grows, there is increasing interest in alternative chemistries beyond the established lithium-ion devices. The lithium–sulfur battery (LSB) is a next-generation energy storage device that boasts a high theoretical specific capacity (1672 mAh g^{-1}) and conventionally utilises a lithium (Li) metal anode in the cell architecture. LSBs promise a low-cost and non-toxic alternative to current lithium-ion battery technology by using readily available sulfur as an active material, instead of transition metal oxides which are often derived from critical minerals and can be toxic and difficult to recycle.[1] Despite the advantages of LSBs, this chemistry unfortunately suffers from

[a]Department of Chemical & Process Engineering, University of Strathclyde, Glasgow, G1 1XJ, UK. E-mail: edward.brightman@strath.ac.uk
[b]Department of Pure & Applied Chemistry, University of Strathclyde, Glasgow, G1 1XL, UK. E-mail: stuart.d.robertson@strath.ac.uk
[c]StorTera Ltd, Edinburgh, EH16 4BB, UK

a series of parasitic reactions, which affect the long-term stability of the cell, termed "polysulfide shuttle".[2,3] The mechanism of this shuttle is debated, but the result is self-discharge of the cell causing irreversible deposition of insoluble, insulative Li_2S onto the anode surface which leads to capacity loss in the cell.[4–6]

A proposed solution to polysulfide shuttle is to use a single liquid flow battery system where sulfur is stored in a catholyte in the form of lithium polysulfides (LiPS), this configuration allows the power and capacity of the system to be independently scaled whilst minimizing the volume of LiPS in the active area of the cell and decreasing self-discharge.[7,8] Another benefit of the LiPS flow cell configuration is the minimisation of the effects of sulfur expansion and contraction at different states-of-charge. Having active material stored in solution, in a tank or reservoir outside the cell, decreases the stress on the cathode structure allowing for more simplistic carbon cathode materials to be used instead of specially designed cathodes which must accommodate for the volume change of the active material. Alongside the cheaper materials that LSBs can utilise, the LiPS flow battery is able to sustain a greater concentration of active material than the typical LSB since it is not restricted by the number of active sites in an electrode structure. In efforts to avoid the formation of elemental sulfur and Li_2S, both of which are insoluble in ether-based electrolytes and highly resistive, the potential window of operation is smaller than traditional LSBs, resulting in a lower theoretical specific capacity of the cell (209 mAh g^{-1}), and hence the LiPS flow battery is best suited to stationary applications. In this work we appraise the LiPS battery chemistry in a coin cell configuration which allows for cheaper and rapid prototyping of electrolyte formulations. These formulations can then be scaled to the flow battery configuration for further optimisation of flow cell specific operation parameters such as flow rate and flow channel design, and to confirm the performance observed by the static cells.

Conventionally the anode of a LiPS battery, or LSB, is typically Li metal, although research is underway into intercalation-conversion anodes for LSBs.[9,10] Using Li metal anodes is desirable due to their high specific capacity (3860 mAh g^{-1}) and low density (0.534 g cm^{-3}) which allow for higher energy density batteries to be formed. Li metal anodes do, however, have the issue of Li dendrite formation which can cause short circuits and safety issues if left unchecked.[11–13] One method of controlling lithium plating is through the formation of a solid-electrolyte interphase (SEI) constructed from decomposed electrolyte and additives such as LiTFSI and $LiNO_3$ which help to control the re-deposition of Li^+ onto the Li metal surface.[14,15] This process requires significant research effort as it is not currently clear which components create the most efficient SEI layer, and the mechanism of the electrolyte decomposition is debated. In a study focusing on lithium metal batteries Ding *et al.* used secondary alkali-metal cations, in the form of $CsPF_6$ and $RbPF_6$, to control the formation of dendrites through a "self-healing electrostatic shield" (SHES) mechanism where the secondary cations make it unfavourable for dendrites to form.[16] Jung *et al.* have shown that the Rb^+ cation can improve the performance of LSBs with lean electrolyte by interacting with both electrodes due to the formation of Rb_2S rather than through the SHES mechanism.[17] In the present study we aim to utilise the benefits of the SHES mechanism and the potential formation of alkali-metal sulfides using alkali-metal bis(trifluoromethylsulfonyl)imides (MTFSI; M = Na, K, Rb, Cs) in a LiPS cell to improve cell performance and longevity. The hexafluorophosphate anion is avoided in this work, as it has been shown to induce ring-opening polymerisation of DOL in typical LSBs,[18] and promote the formation of HF in the presence of even trace amounts of water.[19]

Experimental

Synthesis of alkali-metal bis(trifluoromethylsulfonyl)imide

The MTFSI salts (NaTFSI, KTFSI, RbTFSI & CsTFSI) used in this study were synthesized by a neutralisation reaction of bis(trifluoromethane)sulfonimide (TFSI(H), Sigma-Aldrich, ≥95%, 0.5 M) in methanol (Sigma-Aldrich, ≥99.8%, 10 mL), or ethanol (Fisher Scientific, ≥99.8%, 10 mL), with the respective alkali-metal carbonate (Na_2CO_3: Fisher Scientific, 99.5%; K_2CO_3: Sigma-Aldrich, ≥99.0%; Rb_2CO_3: Sigma-Aldrich, 99% trace metal basis; Cs_2CO_3: Fluorochem, 99%. All alkali-metal carbonates added to solution at 0.25 M) following established procedures.[20,21] Alkali-metal carbonate was slowly added to the dissolved TFSI(H) in alcohol and stirred for 2 h. Alcohol and water were slowly removed by rotary evaporator to leave a white powder, with the final products dried in a vacuum oven at 120 °C overnight before transferring into an Ar-filled glovebox.

Synthesis of LiPS catholyte

Catholyte was synthesized from elemental lithium (Sigma-Aldrich, 99% trace metal basis) and sulfur (Sigma-Aldrich, 99.5%) at a molar ratio of 2 : 6 with sulfur concentration at 2 M. The solid reactants were stored and weighed under an inert atmosphere in an Ar-filled glovebox. A 1 : 1 v/v mixture of 1,2-dimethoxyethane (DME, Fisher Scientific, 99+% stabilised with butylated hydroxytoluene (BHT), anhydrous) and 1,3-dioxolane (DOL, Sigma-Aldrich, 99.8%, anhydrous, ~75 ppm BHT) was added to the solid reactants in a Schlenk flask with a constant supply of Ar gas and refluxed at 65 °C for 24 h. After the solution had cooled, varying concentrations of LiTFSI (Fisher Scientific, 99%, anhydrous) and MTFSI salts alongside 0.3 M $LiNO_3$ (Fisher Scientific, 99%, anhydrous) were added to the catholyte, and left to dissolve for 3 h. All chemicals used in this work were used as received.

Although CsTFSI salt was prepared, it did not dissolve into the DOL/DME electrolyte solution; for this reason, electrochemical testing of this additive was not possible.

Crystallography & characterisation

All crystallographic measurements were made with monochromatic Cu radiation (λ = 1.54184 Å) using a Rigaku Synergy-i diffractometer. Raw data processing utilised the program

CrysalisPro.[22] The structures were refined against F^2 to convergence using all unique reflections and the program Shelxl,[23] as implemented within WinGX.[24] Selected crystallographic and refinement parameters are given in Table S1 and full information in cif format has been deposited with the CCDC as reference numbers 2529359 and 2529360.

^{1}H and ^{13}C NMR spectra were recorded in D_2O on a Bruker AV400 MHz spectrometer operating at 400.13 and 100.62 MHz respectively. ATR-IR spectra were obtained on an Agilent Technologies 550a FTIR spectrometer.

Coin cell assembly

In this study CR2032 coin cells were used for electrochemical characterisation. Coin cells used a Li metal anode (thickness: 0.5 mm; area: 1.77 cm^2; dia. 15 mm) and carbon felt cathode (thickness: 1 mm; area: 1.77 cm^2; dia. 15 mm) with a polypropylene (PP) separator (Shenzhen Mastang Technology Co., Ltd, thickness: 20 μm). Catholyte was pipetted (100 μL) onto the carbon felt. All cell components excluding Li metal and the catholyte were dried in a vacuum oven at 100 °C for 5 h to remove any adhered or absorbed water, and assembled in an Ar-filled glovebox.

Electrochemical characterisation

Galvanostatic charge–discharge (GCD) testing was performed using a Neware CT-4008 battery test system. Cells were cycled for 20 cycles at C/16. All cells were subjected to a 90 minute open circuit potential (OCP) period from the point of assembly prior to cycling to ensure all cells were treated consistently.

Electrochemical impedance spectroscopy (EIS) experiments were performed on a Solartron Analytical EnergyLab XM potentiostat. EIS spectra were measured in potentiostatic mode with a root mean square voltage of 10 mV with frequencies ranging from 100 kHz to 100 mHz. EIS spectra were obtained every 5 minutes during the first 90 minutes after the cell was assembled. The ZView 4 software package has been used to fit the spectra to equivalent circuit models (ECM).

Cyclic voltammetry (CV) experiments were performed on a PalmSens4 potentiostat. The CV measurements were made at a scan rate of 0.05 mV s^{-1} between 1.8 and 3.0 V. The electrolyte used for the CV cells had a lower LiPS concentration of 20 mM, to increase the stability of the response obtained in the CV, while the concentration of all other species remained identical to other electrolytes tested.

Surface analysis

Both the Li metal anode and the carbon felt cathodes have been analysed using scanning electron microscopy (SEM) together with energy dispersive X-ray spectroscopy (EDX) measurements performed on a JEOL JSM-IT800 instrument equipped with a JEOL DrySD EDX spectrometer. All electrodes were rinsed with DME and dried overnight in a glovebox. An inert atmosphere was maintained using an air-free transfer port to the SEM instrument.

Results and discussion

Crystallography

We attempted to recrystallize the alkali-metal TFSI salts from a concentrated DOL/DME solution to determine if there were any interactions with the Lewis basic solvents. This successfully yielded single crystals suitable for X-ray diffraction (XRD) in the case of sodium, potassium and rubidium. The sodium complex (see Fig. 1a, b, S1, S2 and Tables S1–S3 for details) has an empirical formula of TFSINa·DME and crystallises with a dimeric asymmetric unit (Fig. 1a). The sodium cations are coordinated by six oxygen atoms (Fig. S1), coordinating to both a TFSI ligand and a DME molecule in a bidentate fashion to give a six- and five-membered ring respectively, with propagation into a polymer occurring *via* additional Na–O_{TFSI} interactions, utilizing the non-chelating SO units (Fig. 1b & S2) of an adjacent TFSI ligand. The TFSI anion adopts the *cisoid* configuration with respect to their CF_3 groups, with delocalisation of the negative charge through the $N(SO_2)_2$ unit evidenced by the elongation of the SO bonds (ave. 1.430 Å) and contraction of the NS bonds (ave. 1.570 Å) with respect to the more typical double and single bonds of the parent TFSI(H) pro-ligand (1.409/1.644 Å respectively).[25] There is very little difference between Na–O_{TFSI} and Na–O_{DME} bond distances, falling in the narrow range 2.327(6)–2.435(6) Å. All such values are consistent with unsolvated NaTFSI.[26]

The single crystals of the potassium complex returned an identical unit cell to that of unsolvated KTFSI as reported originally by Žák *et al.*[27] and more recently by Roy *et al.*,[28] demonstrating no coordinating role is played by either DOL or DME. This is perhaps unsurprising given the softer nature of potassium although we note that hard O-donors pentaglyme and 18-crown-6 can coordinate KTFSI.[29] Likewise, the rubidium complex crystallizes as an unsolvated polymer (see Fig. 2a, b, S3, S4 and Table S4 for details). This represents, to the best of our knowledge, only the third example of a RbTFSI structure following on from the dioxane[21] and water solvates[20] reported by Pennington *et al.*, which demonstrated that Rb–O coordination is certainly possible. Again, there are two molecules of RbTFSI in the asymmetric unit (Fig. 2a). The Rb centres can be considered to be 9-coordinate, bonding to a total of 6 different surrounding TFSI anions (see Fig. S3 for the relationship of six TFSI anions surrounding a single Rb and Fig. S4 for six Rb cations surrounding a single TFSI anion). Specifically, these are a bidentate TFSI *via* its two SO groups to form a six-membered ring, bidentate *via* an SO_2 group to form a four-membered RbOSO ring, bidentate *via* N and O to form a four-membered RbNSO ring, one monodentate to the in-plane oxygen atom of the aforementioned six membered ring and two monodentate to the out of plane oxygen atoms (Fig. 2b). Charge delocalisation within the TFSI unit is again evident, with contracted SN (ave. 1.578 Å) and elongated SO bonds (ave. 1.434 Å), whilst CF_3 groups are again arranged *cisoid* to one another. Rb–O bonds vary from 2.789(3)–3.327(3) Å, reflecting the variety of

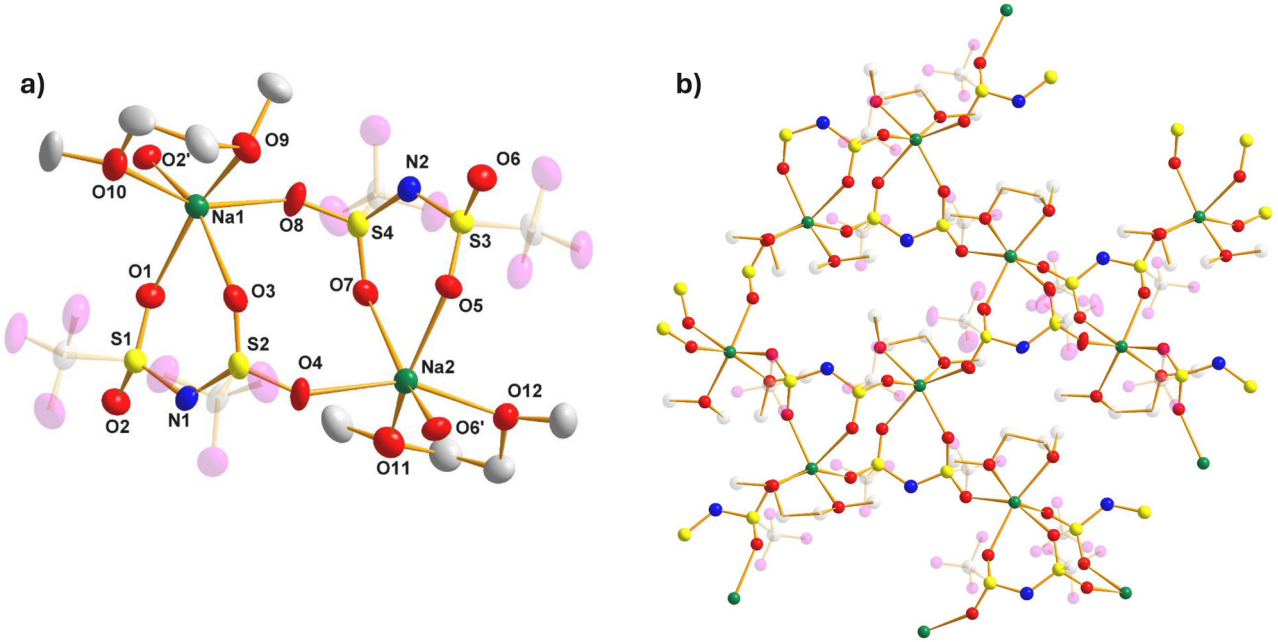

Fig. 1 (a) Asymmetric unit of TFSINa·DME, with hydrogen atoms omitted; (b) structure of TFSINa·DME showing polymer propagation, with hydrogen atoms omitted. All thermal ellipsoids drawn at 50% probability level.

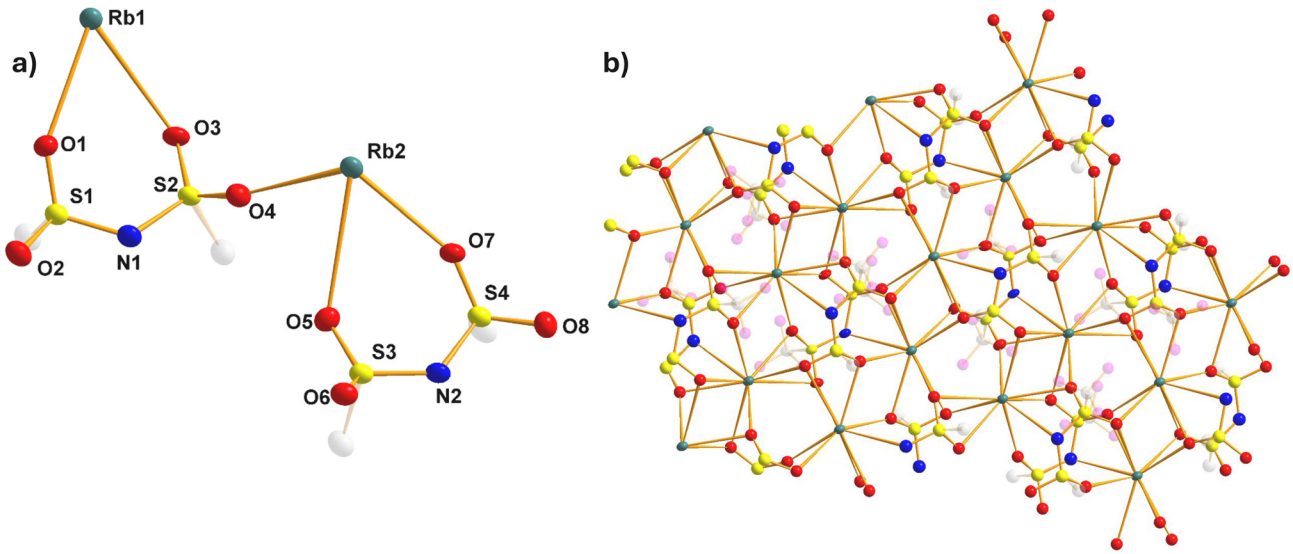

Fig. 2 (a) Asymmetric unit of RbTFSI, with hydrogen and fluorine atoms omitted; (b) structure of RbTFSI showing polymer propagation. All thermal ellipsoids drawn at 50% probability level.

different Rb–O interactions present. The Rb–N interactions (ave. 3.263 Å) are similar to the Cs–N interactions seen in the ten coordinate CsTFSI polymer (3.29(1) Å).[20]

The Cs complex did not provide single crystals suitable for XRD analysis, however a ^{13}C and ^{1}H NMR spectroscopy study (Fig. S5 & S6) suggests that there is no DOL or DME present in the recrystallised material and thus it is highly likely that it forms an unsolvated polymer akin to that published previously.[20]

The Rb complex now completes the family of unsolvated alkali-metal TFSI structures. For completeness, we calculated the Bond Valence Sum (BVS) of the Rb complex for comparison with those discussed for the other alkali-metals by Matsumoto *et al.*[26] BVS (V) estimates the oxidation state of an atom and evaluates the contribution of each individual contact and can be calculated *via* the equation $V = \sum \nu_i = \sum \exp((R_0 - R_i)B)$, where ν_i is the individual bond valence, R_0 = 2.263 Å for Rb–O and 2.37 Å for Rb–N, R_i is the observed bond distance

and B = 0.37 Å.[30] We calculated values of 1.22 and 1.23 for Rb1 and Rb2 respectively (see Tables S5 & S6 for details), which correlate well with Matsumoto's values of 1.06 (Li), 1.17/1.15 (Na), 1.35/0.86 (K) and 1.14 (Cs). Additionally, we calculated a higher BVS for the Na centres on NaTFSI·DME (Na1: 1.30, Na2: 1.27) when compared to the previously reported solvated or unsolvated complexes (Tables S7 & S8).

Cyclic voltammetry

The CVs obtained for each of the MTFSI cells being tested are presented in Fig. 3a. For each MTFSI, two oxidation peaks, an oxidation shoulder and three reduction peaks can be observed. The two overlapping peaks observed around 2.5 V are consistent with what is found in literature,[31] albeit at slightly higher potentials than observed in other works. This is likely due to sulfur being stored in the electrolyte rather than as a solid in the cathode structure, this increases the overpotential as there is less elemental sulfur present. Additionally, the carbon felt used in this work does not have the optimised cathode structures of those used in typical LSBs, which could lead to more sluggish sulfur kinetics. The conversion of elemental sulfur to LiPS can be a sluggish process due to the phase change required and the lack of elemental sulfur present on the cathode could increase the overpotential required for the charge transfer to oxidise LiPS into S_8. The additional oxidation peak above 2.8 V observed in the MTFSI cells cannot be directly attributed to any regular LiPS charge transfer reaction, which leads us to speculate that this peak is related to the alkali-metal and sulfur rich deposits found on each of the MTFSI cell cathodes (Fig. 6), although calculations involving density functional theory would likely be required to confirm.

The reduction peaks occur at similar potentials to that observed in the literature, but the appearance of the CV is quite different. In this work we find an additional reduction peak that varies from 1.9–2.0 V depending on the MTFSI salt and significant overlap between the lower voltage peaks can occur to give the appearance of a single broadened peak which is still in contrast to a typical CV of these materials with sharp peaks observed in those works.[31,32] It is possible that a second LiPS reduction reaction is available in these cells due to the increased amount of LiPS in solution compared to most cells of this kind where LiPS in solution is only formed during the initial reduction at ~2.35 V. $LiNO_3$ has been added to the catholyte used in the CVs to determine if any side reactions occur between the MTFSI salts and $LiNO_3$, throughout the entire voltage window of operation. The addition of $LiNO_3$, or other salts, is not common practice in literature when performing CVs, since the primary goal is often to monitor how the sulfur kinetics change, but by adding $LiNO_3$ we are able to see any potential interactions between the salts that would be present during normal operation of the battery. The presence of $LiNO_3$ explains the cathodic irreversible tail observed around 1.8 V in each of the CVs as this is the approximate onset potential for reduction of $LiNO_3$.[14]

The appearance of the NaTFSI CV is similar to the standard LiTFSI cell with an increased peak intensity at 2.9 V suggesting NaTFSI may allow better utilisation of LiPS in solution. The same result is observed for RbTFSI albeit at decreased intensity. Additionally, for NaTFSI instead of a third reduction peak a pseudo capacitive behaviour is observed, the reason for this is not currently clear. The intensity of both the oxidation and reduction peaks for KTFSI are greatly increased compared to the other salts (Fig. S8) suggesting a possible electrochemical

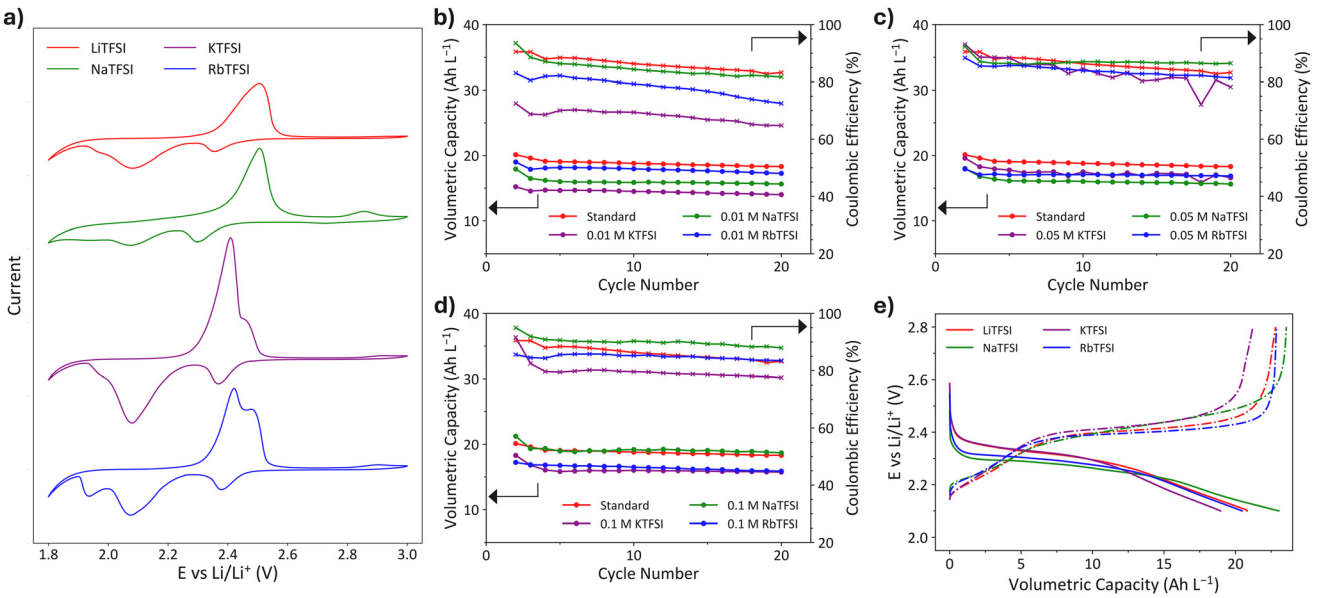

Fig. 3 (a) Stacked CV plot of cells with reduced LiPS concentration (20 mM) containing MTFSI salts compared to a standard LiTFSI cell measured at 0.05 mV s^{-1}, (b–d) discharge capacity (●) and coulombic efficiency (X) for cells with different concentrations of MTFSI: (b) 0.01 M, (c) 0.05 M, (d) 0.1 M; (e) voltage profiles for a typical charge (dashed line) and discharge (solid line) process for different MTFSI salts at 0.1 M.

reaction between KTFSI and the LiPS active material. The third reduction peak is also moved to a higher potential which may prove problematic during the cycling of the cells as more insoluble Li_2S is likely to form. The presence of RbTFSI appears to have the opposite effect with the potential of the third reduction peak being lowered to ~1.9 V and therefore further outside the voltage window used for GCD cycling, meaning that the formation of Li_2S should be less favourable.

Galvanostatic charge–discharge testing

For each of the salts tested, a comparison to a standard static cell with 1 M LiTFSI and 0.3 M $LiNO_3$ was made. The catholytes tested with MTFSI salts had a total $TFSI^-$ anion concentration of 1 M for all cells, alongside 0.3 M $LiNO_3$ (*e.g.* a cell with 0.1 M MTFSI only had 0.9 M LiTFSI). The cells utilised in this study are static CR2032 coin cells which allow for inexpensive and rapid prototyping of different formulations. We have found these cells to be a useful tool for determining salt compatibility and allow screening of formulations without having to produce the larger quantities required for flow cell operation.

In the GCD curves it can be seen that the addition of any MTFSI salt at any concentration decreases the capacity of the cell compared to the standard cell at low discharge rates (Fig. 3b–d), with the exception of Na^+ at 0.1 M. The decreased capacity obtained with most of these salts, whilst undesirable, is not necessarily a drawback as this work is prototyping formulations for a flow battery configuration which allows power and capacity to be scaled independently, so if other performance characteristics can be shown to improve with MTFSI salts then a case for their use could be made, provided similar performance can be achieved in a flow cell.

The addition of Na^+ ions at lower concentrations decreased cell capacity by ~20% from 18–20 Ah L^{-1} which was achieved with the standard formulation (Fig. 3b and c), the coulombic efficiencies of these cells (82–95%) are comparable or greater than the standard (84–90%). At higher concentrations a recovery of the capacity (~19 Ah L^{-1}), compared to the cell with no Na^+ ions, is obtained alongside a further improvement to ~90% of the coulombic efficiency (Fig. 3d). Alongside these improvements, the capacity loss of these cells seems to be slightly less for the cells containing NaTFSI (0.037 Ah per L per cycle–0.068 Ah per L per cycle) compared to the standard cell (0.076 Ah per L per cycle), excluding the first cycle, but extended cycling will be required to confirm long-term implications of this observation.

When K^+ ions are present in solution the performance of the cells is poorer than the standard cell at all concentrations. Although the 0.05 M solution performs relatively better (~18 Ah L^{-1}, 80% coulombic efficiency) compared to the 0.1 M and 0.01 M concentrations (~2–3 Ah L^{-1} and up to 20% decreased coulombic efficiency), (Fig. 3c), all KTFSI-containing cells still underperform relative to the standard. For this reason, finding the optimal K^+ concentration was not considered a productive use of resources. Despite the suspected side reactions between the alkali-metal ions and sulfur for both the KTFSI and RbTFSI additives, the only obvious change in the GCD voltage profile (Fig. 3e) is an increased initial irreversible loss for the Na and Rb salts.

With Rb^+ some improvements in capacity retention are observed (Fig. 3b–d), with less than 0.06 Ah L^{-1} lost per cycle. There is however a reduced capacity of ~1 Ah L^{-1} at 0.01 M which increases to ~2–3 Ah L^{-1} as the Rb^+ concentration increases to 0.1 M, alongside this drop in capacity is a marginally poorer coulombic efficiency. According to the proposed SHES mechanism, RbTFSI was expected to offer the best cell performance of the additives tested due to the increased ionic radii of Rb ions compared to the other alkali-metals tested herein. The larger ionic radius should have provided greater protection from dendrite formation due to an electrostatic repulsion between Rb^+ and Li^+ approaching the Li metal surface. However, since only small enhancements of some characteristics of the cell performance is observed, it suggests that these cells are not limited by the formation of lithium dendrites, or else a side reaction with the Rb^+ cations occurred. A reaction between Rb^+ cations from a $RbNO_3$ additive with sulfur has also been explored by Jung *et al.* in their study on lean electrolyte LSBs, where they establish that the SHES mechanism is not present due to the preferential formation of Rb_2S.[17] It is possible that a similar reaction between the RbTFSI salt and the active material is occurring in these cells.

The theoretical capacity of the cells is 80 Ah L^{-1}, based on the quantity of sulfur active material dissolved in the catholyte. About 25% of this capacity has been achieved by the 0.1 M NaTFSI cell and standard cell, therefore there is sufficient unutilised sulfur available that a side reaction may be occurring without impacting on the capacity of the cells.

As the volume of catholyte was kept constant for each of the cells, the mass of the catholyte used in the cell increases slightly as the alkali-metal present in the salt increases in atomic number. Despite the increased mass this has a small impact on the total mass of solution with a percentage increase compared to the standard of 0.13%, 0.26% and 0.62% for the Na, K, and Rb salts respectively for the highest concentrations of MTFSI salts used. The improvement in capacity obtained for the 0.1 M NaTFSI cell averages at 1.7% with the first cycle having a 5.5% increase compared to the standard cell, therefore the increased cell mass caused by NaTFSI should not be considered as a major factor in the overall efficiency of these cells.

Electrochemical impedance spectroscopy

Since the best performing cells are at higher MTFSI concentrations, the EIS measurements in this work have been performed on the 0.1 M MTFSI cells. The Nyquist plots of the EIS data obtained show the development of the spectra over a 90 minute OCP period prior to cycling (Fig. 4a–d). Due to the 2-electrode cell configuration used, the EIS spectra obtained show charge transfer reactions at both electrodes simultaneously; this can make it difficult to elucidate which physical processes correspond to each feature of the spectrum.

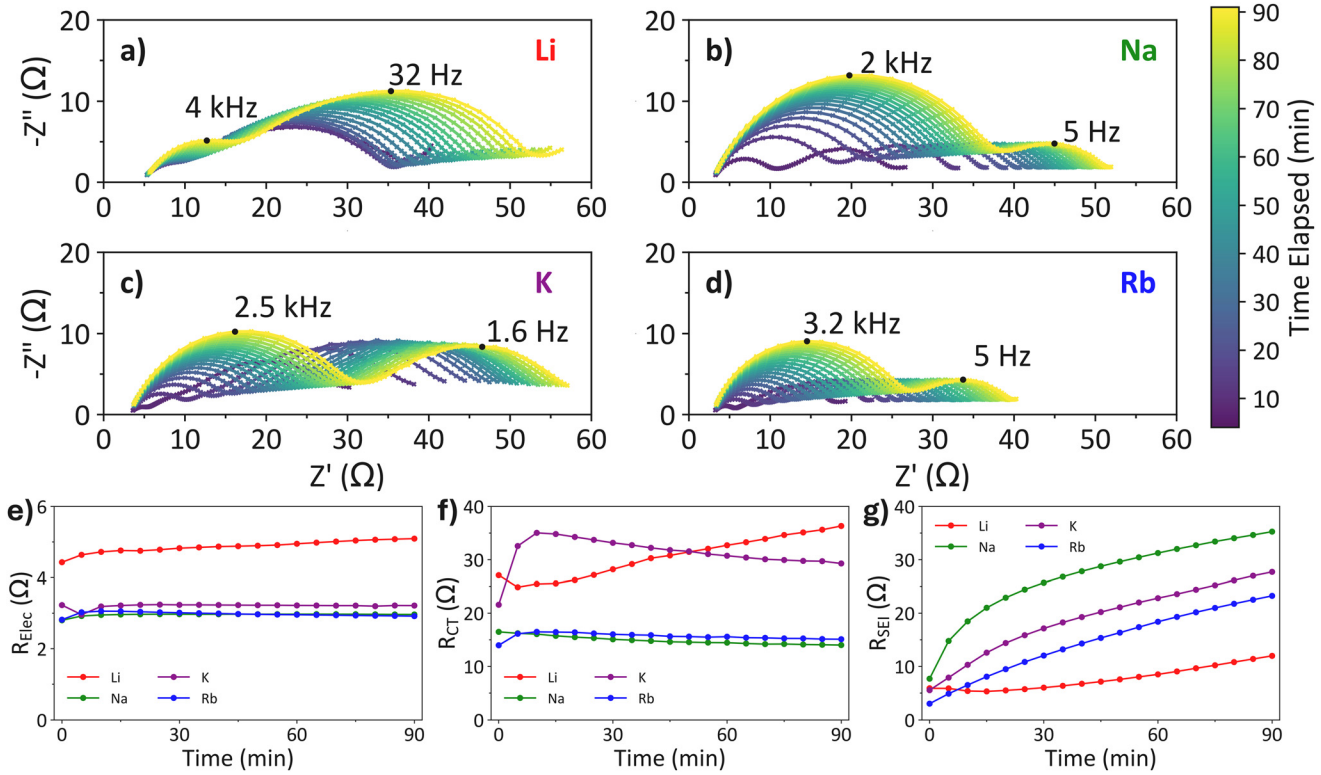

Fig. 4 (a–d) Nyquist plots of EIS data obtained for LiPS cells containing: (a) only LiTFSI; (b) 0.1 M NaTFSI; (c) 0.1 M KTFSI; (d) 0.1 M RbTFSI; (e–g) resistance of different cell components: (e) electrolyte resistance; (f) cathodic charge transfer resistance; (g) SEI layer charge transfer resistance. All resistances calculated from equivalent circuit modelling (see SI Fig. S9 for model details).

However, we have identified two distinct frequency domains for LiPS cells that allow the two electrode contributions to be deconvoluted, and will present this analysis more fully in a future publication. Similar frequency regions have been reported in conventional LSB literature: one region occurs at high frequency (kHz) which corresponds to the diffusion of lithium through the SEI layer;[33] and a low frequency region (Hz) attributed to the charge transfer reactions of LiPS at the cathode.[33–35] A third, low-frequency, domain is present in the sub-Hertz range, which is normally ascribed to diffusion phenomena; only part of this feature was captured in our spectra due to the experimental design prioritising a larger number of scans over capturing the lowest frequency features.

The EIS spectra for the standard cell (Fig. 4a), containing none of the synthesized MTFSI salts, shows increasing resistance from all sources (electrolyte, anode & cathode). This indicates that the additives are continuously being consumed to form an SEI layer on the anode and the loss of conductive ions from solution increases electrolyte resistance. The increasing resistance on the cathode side is suspected to be caused by passivation of the cathode structure, through the formation of elemental sulfur or Li_2S.

The presence of MTFSI greatly affects the performance of the cells and hence changes in the EIS spectra are to be expected. In the Nyquist plots for the EIS spectra of each MTFSI salt (Fig. 4b–d), a decreased ohmic resistance can be observed for each salt by the shift in the spectra to the left compared to the standard EIS spectra, quantified by the fitted R_{Elec} parameter (Fig. 4e), with the NaTFSI cell and RbTFSI cell providing a marginally lower resistance than the KTFSI cell.

The behaviour of the cathodic charge transfer resistance, caused by the charge transfer of LiPS, is altered by the presence of MTFSI salt (Fig. 4f). With NaTFSI and RbTFSI, the growing resistance observed with only LiTFSI is prevented, alongside a general decrease in resistance (Li: 25–38 Ω; Na: 14–16 Ω & Rb: 14–16 Ω), which suggests that an interaction between the MTFSI salts and LiPS, or between the MTFSI salts and the carbon felt, prevents the passivation of the carbon with insulating sulfur or LiPS species. Again, the changes observed for the cathode in a KTFSI cell differs to that seen with the other MTFSI salts: a sudden spike in resistance is observed with KTFSI followed by a gradual relaxation of cell resistance. This observed increase is possibly related to the side reaction observed in the CV for KTFSI (Fig. 3a), where some active material is likely consumed; this could explain the low discharge capacity of the cells containing KTFSI.

The higher frequency semi-circle in each of the Nyquist plots has been attributed to the transport of Li^+ through the SEI layer on the Li anode.[33] For each MTFSI salt the resistance from the Li^+ passing through the SEI is increased compared to LiTFSI only (Fig. 4g). The continually increasing resistance is likely caused by the same mechanism as in the LiTFSI-only

cell, where electrolyte and additives are decomposing to form the SEI layer. The trend observed where the smaller alkali-metal cation has higher resistance could correspond to a feature of the SHES mechanism. If the SHES mechanism is present in this system, then the thin film of M^+ formed will be more tightly packed for smaller ions with smaller ionic radii such as Na^+ compared to larger ions like Rb^+. The more tightly packed layer will more effectively reduce the rate of Li^+ transport through the SEI to the Li anode, thus leading to increased charge transfer resistance.

Scanning electron microscopy

To investigate whether the hypothetical layer of M^+ is present on the Li anode, and to visualise the rest of the SEI layer formed, SEM with EDX analysis was performed on cycled Li anodes in the discharged state (2.1 V). Again, we use a cell containing only LiTFSI and $LiNO_3$ as a standard cell when looking at the composition of the SEI layer (Fig. 5a). On the Li anode of the standard cell a large platelet region (Fig. 5a, red box) is observed composed of sulfur and oxygen likely from the SO group on the TFSI anion as well as some discharged LiPS and decomposed electrolyte. The areas not dominated by the platelet formations show either bare Li substrate (Fig. 5a, black region) or a fluffy fluorine and oxygen region from decomposed TFSI anions (Fig. 5a, blue box). The species found on the Li anode are consistent with those reported in other literature,[36] however it is important to note the absence of nitrogen anywhere on the surface of this anode or any other anode tested in this work (see Fig. S10–S13 for EDX spectra). It is expected that NO_x species should be present on the anode from the $LiNO_3$ which was added in each catholyte with the primary purpose to help form a stable SEI layer.[14,37] The lack of NO_x species on the surface could help explain the low capacity and coulombic efficiencies achieved in this work, as $LiNO_3$ is known to increase cell cycle life by protecting the anode, thus we may be seeing an accelerated degradation of the anode compared to most other studies. A possible explanation for this is the narrower potential range of cycling in our system compared to conventional LSB work, as the reduced voltage window may alter how $LiNO_3$ is being utilised in the cell. By preventing the formation of high concentrations of short chain insoluble LiPS it is possible that $LiNO_3$ is being consumed *via* a different mechanism. This would appear to be the case as nitrogen species are detected on the cathodes

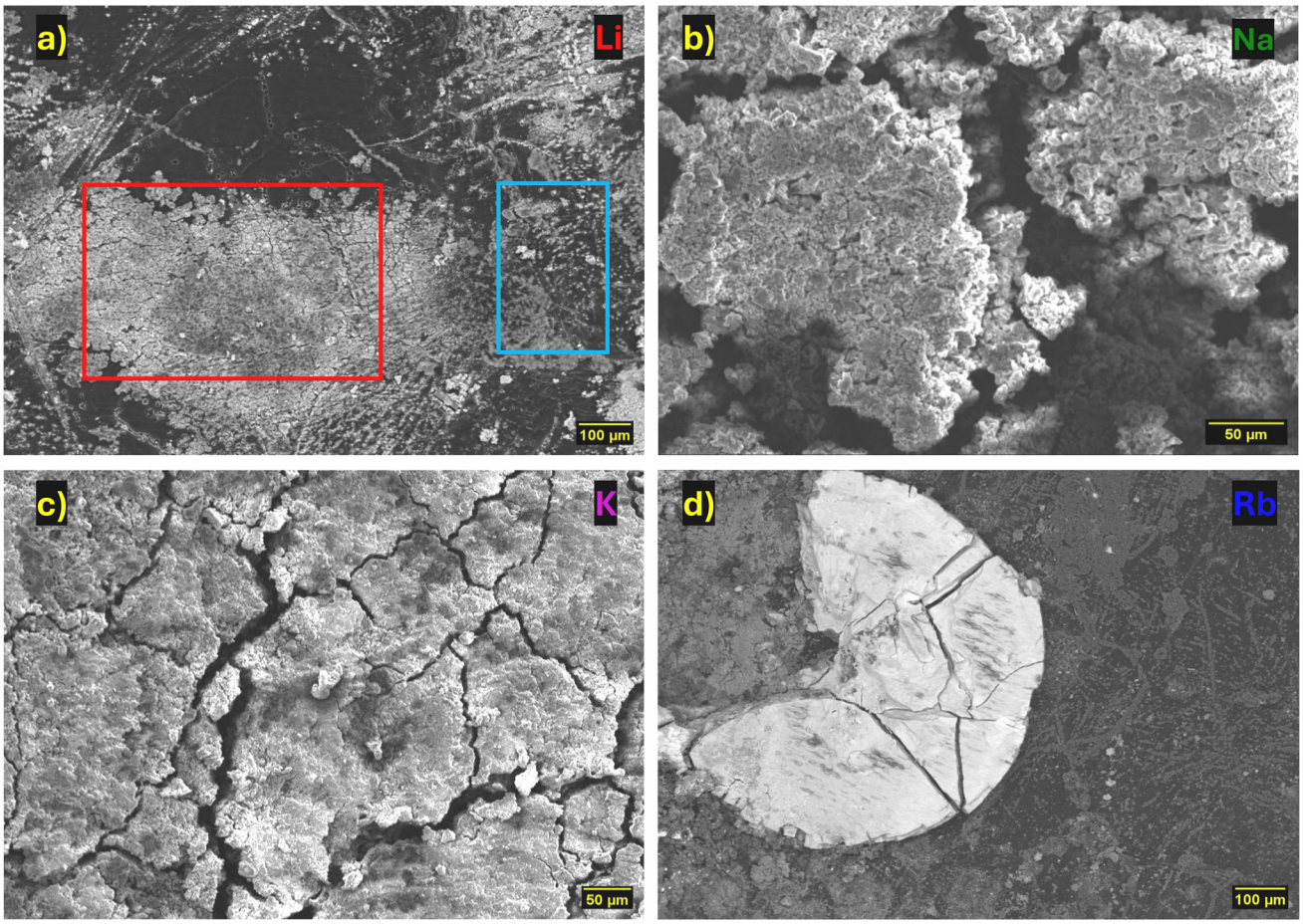

Fig. 5 (a–d) SEM images of the Li anode from cells containing: (a) only LiTFSI; (b) 0.1 M NaTFSI; (c) 0.1 M KTFSI; (d) 0.1 M RbTFSI. EDX spectra and element mapping for each sample are shown in SI Fig. S10–S13.

(Fig. S15c & S16c), however, a more detailed mechanistic study involving *operando* spectroscopic methods would be required to verify this, which is outside the scope of this work. The apparent change in the behaviour of $LiNO_3$ within the cell cannot be directly attributed to the presence of MTFSI since the anode from the standard cell also lacks any NO_x species.

The MTFSI anodes mostly have a similar appearance to the LiTFSI-only anode with the addition of a trace of Na or K for cells containing the respective MTFSI (Fig. 5b–d). In addition to the trace amounts of Rb on the surface, large clusters (~800 μm) containing rubidium and sulfur are found alongside a reduced amount of sulfur in the platelet region compared to the other anodes, this is possibly evidence of the parasitic reaction between rubidium and sulfur that could be the cause of reduced capacity especially if the deposits are irreversibly formed. Due to the absence of bonding information obtained from SEM-EDX analysis it cannot be stated conclusively that the deposits are alkali-metal sulfides, although the presence of the deposits does correlate well with that observed by Jung *et al.* where a layer of Rb_2S is formed on both anode and cathode surfaces.[17] However, the deposits in our work seem to prefer a clustered formation rather than a more uniform layer.

The appearance of alkali-metal deposits on the anode surface is evidence that the SHES mechanism is likely not occurring in this system as a dominant reaction for the alkali-metal ions. The formations of alkali-metal deposits suggest a reaction between the alkali-metals and the active material which may offer some beneficial cycling properties but unfortunately comes at the expense of useable active material available for cycling the cell.

In addition to the anodes, the carbon felt cathodes (in the discharged state) have also been analysed using SEM-EDX (Fig. 6, EDX spectra in Fig. S14–S17). The cathode from the LiTFSI cell had small clusters containing sulfur, oxygen and fluorine on the individual strands of the felt (Fig. 6a, red arrows). With the addition of MTFSI the behaviour of species on the carbon surface appears to be altered significantly and some variation occurs from one alkali-metal to another. When Na is present the surface of the felt is coated in a layer of

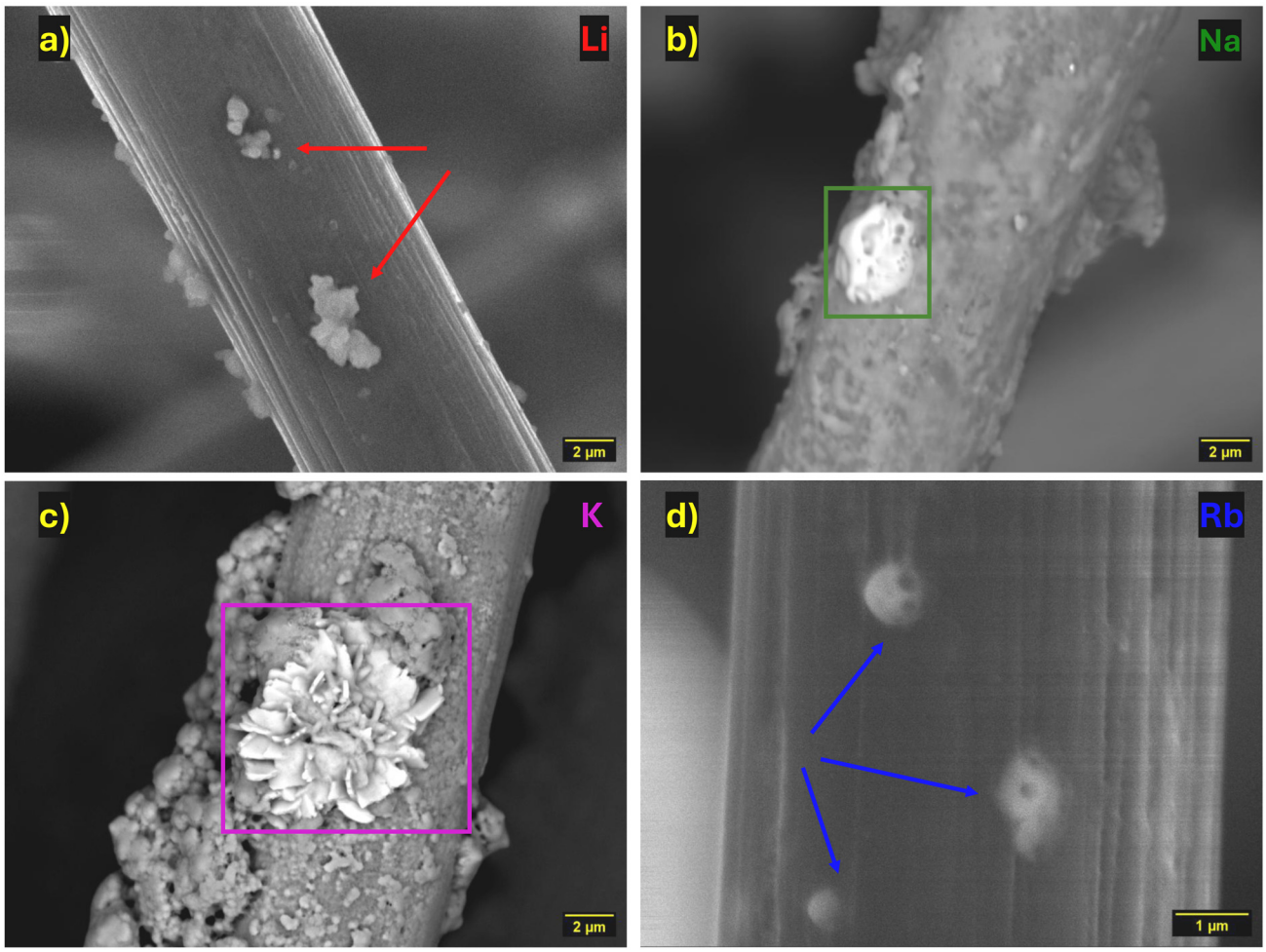

Fig. 6 (a–d) SEM images of the carbon felt cathodes from cells containing: (a) only LiTFSI; (b) 0.1 M NaTFSI; (c) 0.1 M KTFSI; (d) 0.1 M RbTFSI. EDX spectra and element mapping for each sample are shown in SI Fig. S14–S17.

sodium, oxygen, fluorine, sulfur and nitrogen. This layer shows that likely most of the nitrate added into the system has remained on the cathode side of the cell forming a cathode-electrolyte interphase. In addition, evidence of a potentially parasitic side reaction can be found in the cluster of sodium and sulfur (1–2 μm) on the carbon felt (Fig. 6b, green box). The same effects can be observed on the KTFSI cell cathode but are more pronounced (Fig. 6c). The larger clusters (~3 μm) formed on the cathode take on a floral structure with high concentrations of potassium and sulfur (Fig. 6c, pink box), this provides more evidence of a significant side reaction between the KTFSI and the LiPS active material. The cathode from the RbTFSI cell again has a coating of oxygen, fluorine and sulfur alongside rubidium and the presence of alkali-metal formations on the felt (Fig. 6d, blue arrows). These formations take on a smaller and more spherical shape (~0.5 μm) whilst appearing to be embedded into the carbon rather than attached to the surface.

Conclusions

In this research we have synthesised alkali-metal TFSI salts for use as a co-additive in LiPS batteries alongside more traditional additives. These co-additives offer improvements in key performance parameters, such as capacity, capacity retention and coulombic efficiency, at high concentrations (0.1 M) of the sodium and rubidium salts. Additionally, through single crystal XRD we report the first example of solvent-free RbTFSI, continuing and completing the family of unsolvated alkali-metal TFSI complexes. It was initially hypothesised that cells would benefit from MTFSI additives due to the SHES mechanism, previously reported by Ding *et al.*, but clear evidence is provided of side reactions between the MTFSI salts and the LiPS active material, established through electrochemical methods and surface analysis of the electrodes. Since improvements in performance can be observed for both NaTFSI and RbTFSI despite a loss of active material from the side reactions, an argument can be made for the use of secondary cations in both LSBs and LiPS batteries although further investigation to optimise the counter anion and additive concentration is required. Additionally, the additives should be tested in a flow battery configuration to confirm the findings of the static cell. Alongside being one of the better performing salts, NaTFSI is currently commercially available, due to its use in sodium-ion chemistries, which may make it a more appealing choice over more bespoke additives for industry.

Author contributions

Thomas J. Leckie: conceptualization, methodology, investigation, data curation, writing – original draft, writing – review & editing, visualization. Calvin N. Turner: methodology, investigation. Alan Kennedy: validation – crystallography, formal analysis – crystallography, resources, data curation. Niall Dalton: writing – review & editing, supervision. Pasidu Pallawela: supervision, funding acquisition. Stuart D. Robertson – conceptualization, methodology, data curation, writing – original draft, writing – review & editing, visualization, supervision, project administration. Edward Brightman: conceptualization, resources, writing – review & editing, supervision, project administration, funding acquisition.

Conflicts of interest

There are no conflicts to declare.

Data availability

Data supporting the findings of this work are available at the University of Strathclyde at the following link https://doi.org/10.15129/ddc5269b-dd70-4fc6-9327-18c037eb5664.

Supplementary information (SI) including further crystal structure data, NMR and FTIR spectroscopy, and SEM-EDX maps is available. See DOI: https://doi.org/10.1039/d6eb00050a.

CCDC 2529359 and 2529360 contain the supplementary crystallographic data for this paper.[38a,b]

Acknowledgements

We thank EPSRC Doctoral Training Partnership DTP 2224 (EP/W524670/1) and StorTera Ltd for a PhD scholarship for T. J. L. Additionally, we thank Dr Aaron B. Naden from the University of St Andrews Electron Microscopy Facility for performing & training T. J. L. in SEM analysis. We acknowledge the EPSRC Light Element Analysis Facility Grant (EP/T019298/1) and the EPSRC Strategic Equipment Resource Grant (EP/R023751/1).

References

1 A. Iqbal, A. Kakoria, S. T. Riaz, J. Xu, R. I. Pushparaj and G. Xu, *J. Power Sources*, 2025, **655**, 237914.
2 D. Moy, A. Manivannan and S. R. Narayanan, *J. Electrochem. Soc.*, 2014, **162**, A1.
3 N. Xu, T. Qian, X. Liu, J. Liu, Y. Chen and C. Yan, *Nano Lett.*, 2017, **17**, 538–543.
4 P. Schön, F. Hintz and U. Krewer, *Electrochim. Acta*, 2019, **295**, 926–933.
5 Q. Zou and Y.-C. Lu, *J. Phys. Chem. Lett.*, 2016, **7**, 1518–1525.
6 D. Blanchard and M. Slagter, *JPhys Energy*, 2021, **3**, 044003.
7 K. J. Siczek, in *Next-Generation Batteries with Sulfur Cathodes*, ed. K. J. Siczek, Academic Press, 2019, pp. 193–199.
8 K. Dong, S. Wang and J. Yu, *RSC Adv.*, 2014, **4**, 47517–47520.

9 W. Yao, J. Xu, Y. Cao, Y. Meng, Z. Wu, L. Zhan, Y. Wang, Y. Zhang, I. Manke, N. Chen, C. Yang and R. Chen, *ACS Nano*, 2022, **16**, 10783–10797.
10 V. P. Nguyen, Y. Qureshi, H. C. Shim, J. M. Yuk, J.-H. Kim and S.-M. Lee, *Small Struct.*, 2024, **5**, 2400196.
11 J. Jiang, Z. Lu, Y. Ding, S. Liu, Z. Qi, T. Tang, Y. Zhang, Z. Ma, J. Sun, L. Xue, W. Zhang, P. Xiong, X. Wang, J. Zhu and Y. Fu, *J. Energy Chem.*, 2025, **100**, 674–683.
12 J. Wang, S. Yi, J. Liu, S. Sun, Y. Liu, D. Yang, K. Xi, G. Gao, A. Abdelkader, W. Yan, S. Ding and R. V. Kumar, *ACS Nano*, 2020, **14**, 9819–9831.
13 S. Han, J. H. Lee, J. Kim and J. Lee, *Discover Chem. Eng.*, 2024, **4**, 9.
14 S. S. Zhang, *Electrochim. Acta*, 2012, **70**, 344–348.
15 H. Zhang, C. Shen, Y. Huang and Z. Liu, *Appl. Surf. Sci.*, 2021, **537**, 147983.
16 F. Ding, W. Xu, G. L. Graff, J. Zhang, M. L. Sushko, X. Chen, Y. Shao, M. H. Engelhard, Z. Nie, J. Xiao, X. Liu, P. V. Sushko, J. Liu and J.-G. Zhang, *J. Am. Chem. Soc.*, 2013, **135**, 4450–4456.
17 J. Jung, H. Cho, I. Kim, S. Kim, W. Jo and H.-T. Kim, *Energy Storage Mater.*, 2023, **63**, 103040.
18 M. Xie, Y. Wu, Y. Liu, P. P. Yu, R. Jia, W. A. Goddard and T. Cheng, *Mater. Today Energy*, 2021, **21**, 100730.
19 D. Zhu, L. Sheng, T. Hu, S. Chen, M. Shi, H. Hua, K. Yang, J. Wang, Y. Tang, X. He and H. Xu, *J. Phys. Chem. Lett.*, 2024, **15**, 4024–4030.
20 L. Xue, C. W. Padgett, D. D. DesMarteau and W. T. Pennington, *Solid State Sci.*, 2002, **4**, 1535–1545.
21 L. Xue, C. W. Padgett, D. D. DesMarteau and W. T. Pennington, *Acta Crystallogr., Sect. C: Struct. Chem.*, 2004, **60**, m200–m202.
22 CrysalisPRO, Rigaku Oxford Diffraction Ltd, Yarnton, England, 2016.
23 G. M. Sheldrick, *Acta Crystallogr., Sect. C: Struct. Chem.*, 2015, **71**, 3–8.
24 L. J. Farrugia, *J. Appl. Crystallogr.*, 2012, **45**, 849–854.
25 A. Haas, Ch. Klare, P. Betz, J. Bruckmann, C. Krüger, Y.-H. Tsay and F. Aubke, *Inorg. Chem.*, 1996, **35**, 1918–1925.
26 K. Matsumoto, T. Matsui, T. Nohira and R. Hagiwara, *J. Fluor. Chem.*, 2015, **174**, 42–48.
27 Z. Žák, A. Růžička and Ch. Michot, *Z. Kristallogr. – Cryst. Mater.*, 1998, **213**, 217–222.
28 E. Nag, S. Battuluri, K. C. Mondal and S. Roy, *Chem. – Eur. J.*, 2022, **28**, e202202324.
29 T. Mandai, K. Yoshida, S. Tsuzuki, R. Nozawa, H. Masu, K. Ueno, K. Dokko and M. Watanabe, *J. Phys. Chem. B*, 2015, **119**, 1523–1534.
30 I. D. Brown and D. Altermatt, *Acta Crystallogr., Sect. B: Struct. Sci.*, 1985, **41**, 244–247.
31 R. Liu, Z. Wei, L. Peng, L. Zhang, A. Zohar, R. Schoeppner, P. Wang, C. Wan, D. Zhu, H. Liu, Z. Wang, S. H. Tolbert, B. Dunn, Y. Huang, P. Sautet and X. Duan, *Nature*, 2024, **626**, 98–104.
32 G. Tan, R. Xu, Z. Xing, Y. Yuan, J. Lu, J. Wen, C. Liu, L. Ma, C. Zhan, Q. Liu, T. Wu, Z. Jian, R. Shahbazian-Yassar, Y. Ren, D. J. Miller, L. A. Curtiss, X. Ji and K. Amine, *Nat. Energy*, 2017, **2**, 17090.
33 M. Adamič, S. D. Talian, A. R. Sinigoj, I. Humar, J. Moškon and M. Gaberšček, *J. Electrochem. Soc.*, 2018, **166**, A5045.
34 X. Qiu, Q. Hua, L. Zheng and Z. Dai, *RSC Adv.*, 2020, **10**, 5283–5293.
35 H. Fazal, D. Eroglu, A. Kilic, N. Ali, C. Yan, J. Zai and X. Qian, *ChemElectroChem*, 2024, **11**, e202300781.
36 F. Jiang, Y.-F. Du, J.-X. Guo, N.-L. Shen, Z.-X. Chen, M. Geng, D. Ren, B.-Q. Li, X.-Q. Zhang, T. Wang, Y. Ma, Y. Zhong, J. He, Z. Zhu, F. Wang, J.-Q. Huang, X.-B. Cheng and Y. Wu, *Energy Environ. Sci.*, 2025, **18**, 4925–4933.
37 L. Wu, J. Hu, S. Chen, X. Yang, L. Liu, J. S. Foord, P. Pobedinskas, K. Haenen, H. Hou and J. Yang, *Electrochim. Acta*, 2023, **466**, 142973.
38 (*a*) CCDC 2529359: Experimental Crystal Structure Determination, 2026, DOI: 10.5517/ccdc.csd.cc2qx07x; (*b*) CCDC 2529360: Experimental Crystal Structure Determination, 2026, DOI: 10.5517/ccdc.csd.cc2qx08y.